MŰEGYETEM 1782

BUDAPEST UNIVERSITY OF TECHNOLOGY AND ECONOMICS

FACULTY OF MECHANICAL ENGINEERING

DEPARTMENT OF FLUID MECHANICS

Kinga Andrea Kovács

Vortex detection in three-dimensional flows around solid bodies

TDK Study

Advisor: Dr. Esztella Balla
Assistant professor
Department of Fluid Mechanics

Budapest, 2023

Table of contents

Nomenclature

Latin letters	**Name**	**Unit**
$B(t)$	Boundary of a rotationally coherent Lagrangian vortex	
c	Chord length	m
c_D	Drag coefficient	-
c_L	Lift coefficient	-
C	Courant number	-
$C(t)$	Center of a rotationally coherent Lagrangian vortex	
d	Diameter	m
$D(t)$	Rotationally coherent Lagrangian vortex	
f	Vortex shedding frequency	Hz
h	Height of the cylinder	m
$L(t)$	Lagrangian coherent structure	
Q_V	Volume flow rate	$m^3 \cdot s^{-1}$
Δp_s	Static pressure rise	Pa
r_b	Blade tip radius	m
Re	Reynolds number	-
s	Variable of integration	
Sr	Strouhal number	-
t	Final time instant of the integration	s
t_0	Starting time instant of the integration	s
Δt	Time step size	s
u	Blade tip peripheral velocity	$m \cdot s^{-1}$
V	Velocity magnitude	$m \cdot s^{-1}$
$\boldsymbol{v}(\boldsymbol{x},t)$	Unsteady velocity field	$m \cdot s^{-1}$
$\boldsymbol{x}(t,\boldsymbol{x}_0)$	Instantaneous particle positions	m
$\boldsymbol{x}_0$	Initial particle positions	m
Δx	Smallest cell size in the domain in the direction of the flow	m
Δx_{ij}	Difference between the centers of the neighboring vortices in the *x*-direction	m

Δy_{ij}	Difference between the centers of the neighboring vortices in the y-direction	m

Greek letters	Name	Unit
μ	Dynamic viscosity	$kg \cdot m^{-1} \cdot s^{-1}$
ρ	Density	$kg \cdot m^{-3}$
Φ	Global flow coefficient	-
Ψ	Global static pressure rise coefficient	-
$\boldsymbol{\omega}(\boldsymbol{x},t)$	Vorticity	s^{-1}
$\overline{\boldsymbol{\omega}}(t)$	Instantaneous spatial mean of the vorticity	s^{-1}

Abbreviations		Unit
CFD	Computational Fluid Dynamics	
DeficiencyThresh	Convexity deficiency threshold	%
LAVD	Lagrangian-averaged vorticity deviation	-
LE	Leading edge	
MinLength	Minimal arc-length threshold	%
Nct	Number of contour levels	-
ODE	Ordinary Differential Equation	
RMS	Root mean square	SI
TE	Trailing edge	
TLV	Tip leakage vortex	

1 Introduction and objectives

Extensive research has been dedicated to studying the flow around solid objects, driven by the wide range of practical uses. For instance, according to [1] many structural elements and civil structures have rectangular sections. In the case of these bluff bodies, aerodynamic instability phenomena such as vortex-induced vibration and galloping are usual. These phenomena have to be accounted for when estimating wind loading and aeroelastic instability for these sections. Studies in connection with this type of geometry have typically been conducted by means of wind tunnel measurements and Computational Fluid Dynamics (CFD) simulations. As for another example, in [2] it is stated that wind is one of the dominant load criteria in the design of tall circular chimneys which are important power plant structures. Vortex induced oscillations significantly influence the across-wind load and response of a chimney. In [2] a full scale experiment was examined in connection with the mentioned structure.

When it comes to bluff bodies, there is a specific range of the Reynolds number where the so-called von Karman vortex street phenomenon occurs [3]. This phenomenon is characterized by symmetric and periodic vortex shedding. The said flow pattern can sometimes trigger unwanted structural vibrations which can become especially hazardous when the frequency of vortex shedding coincides with the natural frequencies of the bodies [3]. Consequently, engineers need to give careful thought to the impact of vortex shedding when designing buildings like skyscrapers and chimneys to reduce potential risks.

Previous vortex detection research has already been performed by the author in connection with a two-dimensional circular cylinder, and a two-dimensional square cylinder for various Reynolds numbers and/or angles of attack [4]. The applied vortex detection method was the so-called Lagrangian-averaged vorticity deviation (LAVD) vortex identification method, which is based on [5]. The main result of the study was the detection of vortices, the identification of the main vortex detection parameters (recommendations were given for their values) which fundamentally determine the outcome of the detection, and the comparison of the detected vortices with other detection results.

In the current study the author aims to perform the vortex detection (with the LAVD method), and the parameter identification for a three-dimensional circular cylinder geometry. The repeated parameter identification of the LAVD method is vital because the publication on which the LAVD method is based [5], does not give suggestions for the values of the parameters, thus, decreasing the practicality, and applicability of the method. By performing the parameter identification repeatedly for different cases, a more general view can be obtained in connection with the parameters, and more general suggestions can be formulated for the settings of the LAVD vortex detection method. The data for which the detection is performed is a result of simulation, which was performed using ANSYS Workbench 2023 R2 [6]. Two simulations were run for two different Reynolds numbers. The vortex detection was performed using MATLAB 2023a [7]. A comparison of the current suggested parameter values with the previously obtained results [4] will also be presented.

Apart from the circular cylinder geometry, the capabilities of the LAVD method is tested on a case study of an axial flow fan. To the author's best knowledge this is the first application of this method on flows produced by turbomachinery. According to [8] low-speed axial fans are frequently used both in industrial and household applications, therefore, high-efficiency and low-noise emission are very important characteristics. However, one of the main sources of losses, and noise emission is the tip leakage flow [8]. The lip leakage flow can cause almost a third of the hydraulic losses, and in many cases, it has been identified as the dominant sound source [8]. For axial flow fans, the tip leakage flow rolls up and forms the tip leakage vortex (TLV) [8]. After the rollup, the TLV core starts spiraling as it propagates downstream in the blade passage.

In the current study the author aims to detect the tip leakage vortex cores in the case of an axial fan by applying the LAVD vortex identification method. The data for which the detection is performed is a result of simulation, presented in [9]. According to [9] the simulation was performed using the ANSYS Fluent 22R2 software. Comparison of the detection results will also be performed with results provided by a different author (Bálint Lendvai). In said case, the detection was carried out by Banks' vorticity predictor-pressure corrector vortex core identification method.

2 Lagrangian-averaged vorticity deviation

2.1 Theoretical background

As it was already mentioned, the applied vortex detection method is the so-called Lagrangian-averaged vorticity deviation (LAVD) which is proposed in [5]. According to [5], the definition of coherent vortices is still a disputed matter, however there are two main characteristics which are widely accepted:

1. Vortices are concentrated regions of high vorticity
2. Vortices are generally viewed as evolving domains with a high level of material invariance

Despite the fact that these characteristics are broadly accepted, different authors interpret vortices in different ways. In [5] an objective vortex criterion is proposed, this is the so-called

Lagrangian-averaged vorticity deviation (LAVD). The Lagrangian-averaged vorticity deviation is defined as the integral of the normalized difference between the vorticity and its spatial mean over a trajectory [5].

Mathematically, it can be expressed as:

$$LAVD_{t_0}^{t}(\boldsymbol{x}_0) \coloneqq \int_{t_0}^{t} |\boldsymbol{\omega}(\boldsymbol{x}(s;\boldsymbol{x}_0),s) - \overline{\boldsymbol{\omega}}(s)|ds \tag{1}$$

Where t_0 [s] is the starting time instant of the integration, t [s] is the final time instant of the integration, $\boldsymbol{x}_0$ [m] denotes the initial particle positions, $\boldsymbol{\omega}(\boldsymbol{x},s)$ $\left[\frac{1}{\mathrm{s}}\right]$ is the vorticity, $\boldsymbol{x}(s;\boldsymbol{x}_0)$[m] denotes the instantaneous particle positions, s is the variable of integration, and $\overline{\boldsymbol{\omega}}(s)$ $\left[\frac{1}{\mathrm{s}}\right]$ is the instantaneous spatial mean of the vorticity.

According to [5] a Lagrangian vortex is a nested set of material tubes with outward decreasing tubular level sets of LAVD. The LAVD is derived from the dynamic rotation tensor, which is obtained from the dynamic polar decomposition of the deformation gradient. This provides an objective global vortex criterion which is entirely frame-invariant.

The use of LAVD allows for the objective detection of material tubes, along which small fluid volumes exhibit the same bulk rotation compared to the mean rotation of the fluid [5]. The initial positions of these tubes correspond to tubular level surfaces of the $LAVD_{t_0}^{t}(\boldsymbol{x}_0)$. In 2D, these tubular sets can be interpreted as closed convex curves, while in 3D, they can be understood as convex, cylindrical, cup-shaped, or toroidal sets [5].

According to [5], a rotationally coherent Lagrangian vortex must satisfy the following conditions:

1. It is an evolving material domain $D(t)$ where $D(t_0)$ is filled with tubular level surfaces of $LAVD_{t_0}^{t}(\boldsymbol{x}_0)$ and the LAVD values are decreasing as one moves outwards
2. The boundary $B(t)$ of $D(t)$ is a material surface where $B(t_0)$ is the outermost tubular level surface (minimum) of $LAVD_{t_0}^{t}(\boldsymbol{x}_0)$ in $D(t_0)$
3. The center $C(t)$ of $D(t)$ is a material set where $C(t_0)$ is the innermost member (maximum) of $LAVD_{t_0}^{t}(\boldsymbol{x}_0)$ in $D(t_0)$

In Fig. 1 a rotationally coherent Lagrangian vortex can be seen. The first figure is at the beginning of the examined time interval and the second figure represents the current state. *L(t)* represents a rotational Lagrangian coherent structure, this means that along *L(t)* fluid volumes have the same rotation in the given time interval.

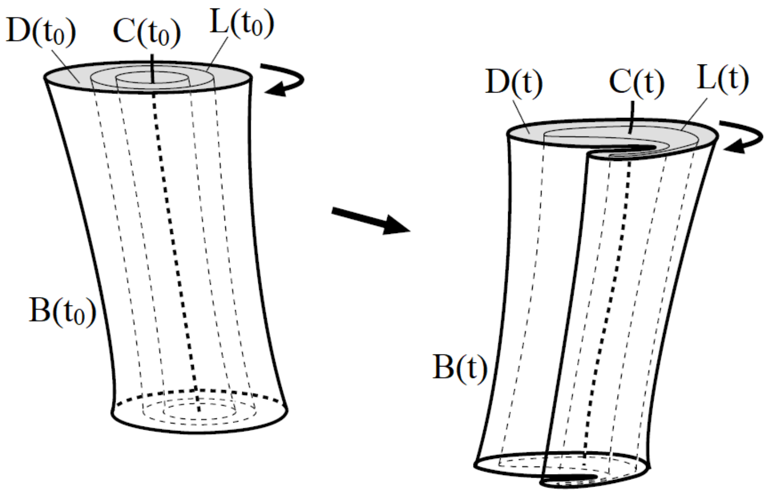

Fig. 1 Initial and current positions of a Lagrangian vortex *D(t)*;
(reproduced from [5])

2.2 Numerical implementation

In this section the numerical implementation of the three-dimensional LAVD method will be discussed briefly. It is important to note that some modifications were made in connection with the freely accessible code. The major problem was that the original code was intended to be used for equidistant, uniform grid data, however, in the case of fluid dynamics, uniform grid data is seldom available, on the other hand, scattered data is much more usual (e.g. in the case of CFD simulations). The interpolation of the velocity data is needed during the calculations (detailed later), however, the 'scatteredInterpolant' function of MATLAB can only interpolate up to three dimensions (due to the transient aspect of the flow, a four-dimensional scattered interpolation is required), consequently, the interpolation had to be reformulated within the MATLAB code.

The first step is to create a uniform grid, in order to be able to perform the interpolation later on. Afterwards, the interpolation functions have to be created for the interpolation of the velocity values which were exported from the CFD simulation. This was done in the following way: an interpolation function was created for each velocity component and for each time step. For example, in the case of 20 time steps this would mean 60 interpolation functions in total. As a next step, the following ordinary differential equation (ODE) has to be solved to calculate the particle trajectories:

$$\frac{dx}{dt} = \boldsymbol{v}(\boldsymbol{x}, t) \tag{2}$$

The ODE is solved by using the built-in 'ode45' function, and the initial particle positions correspond to the created uniform grid. The vorticity values are then subsequently integrated along the trajectories. With the help of the vorticity values, the LAVD matrix can be determined with Eq. (1).

As for the contour extraction, it is important to mention that in the three-dimensional case as well (similarly to the two-dimensional case), the vortices are sought in different two-dimensional planes, these said planes can be selected. At first, the local maxima of the LAVD field are identified. All of the LAVD level curves in the vicinity of the maxima have to be extracted. The vortex boundary is identified as the outermost convex LAVD level. These levels are only extracted as long as the value of the LAVD decreases outward from the vortex center. The general outputs of the code are the coordinates of the vortex centers and the coordinates of the vortex boundaries.

3 Circular cylinder

3.1 Simulation setup

The three-dimensional cylindrical domain (which is representing the fluid domain) was constructed using SpaceClaim [6] and DesignModeler [6]. A cylindrical shape was cut out of the domain, which is representing the infinitely long cylinder. The geometry had to be split into several parts so that later on a structured, hexahedral mesh could be created.

The diameter (d) and the height (h) of the cylinder are the following:

$$d = 0.01\ [\mathrm{m}] \tag{3}$$

$$h = 0.06\ [\mathrm{m}] \tag{4}$$

The circular domain has a dimension of 40 diameters, and its height is equal to the height of the cylinder (h). The geometrical model is based on [10] and can be seen in Fig. 2.

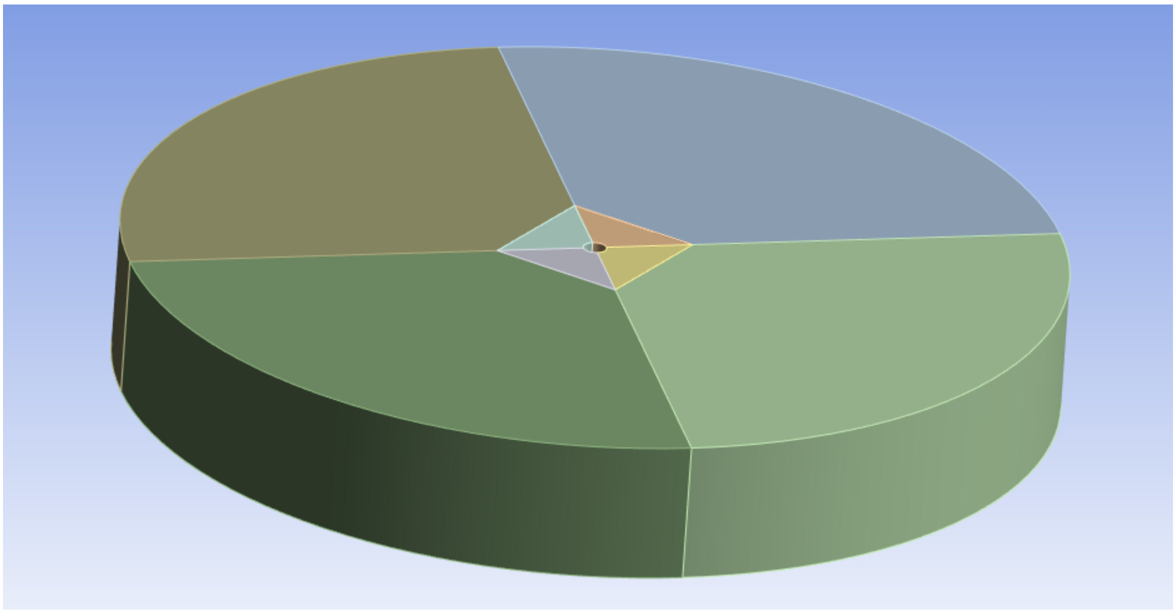

Fig. 2 The constructed geometrical model.

The meshing is also based on [10], and it was performed in the Ansys Workbench Mesher [6], where a structured, hexahedral mesh was created. The MultiZone method was applied with Hexa elements. There are 140, 120, and 32 nodes stretched along the radial, the circumferential, and the vertical directions, respectively.

The appropriate resolution of the mesh was also achieved by applying appropriate biases along with the sizings. The mesh was more refined in the regions close to the cylinder so that the simulations could capture the vortex shedding effects appropriately. The smallest cell size in the domain is approximately $4.5\cdot10^{-4}$ [m], and the mesh consists of 558,360 nodes. The mesh quality was checked by inspecting the maximum and average values of the skewness attribute, these are the following:

$$skewness_{max} = 0.50\ [-] \tag{5}$$

$$skewness_{average} = 0.13\ [-] \tag{6}$$

The quality of the mesh is satisfactory, because for hexahedral elements the maximum skewness should not exceed 0.85 [11]. It can be seen that this requirement has been fulfilled. In Fig. 3 and Fig. 4 the generated mesh can be seen.

Two simulations were run for two different Reynolds numbers (60 and 100) using Ansys Fluent 2023 R2 [6]. With respect to the $Re = 100$ case, the aim was to visualize the so-called von Karman vortex street phenomenon, which is characterized by symmetric and periodic vortex shedding [12]. As for the $Re = 60$ case, for this Reynolds number a laminar, unstable wake can be observed (the vortex shedding phenomenon is present here as well) [12]. From the Reynolds number the inlet velocity can be calculated in the following way [3]:

$$Re = \frac{V \cdot \rho \cdot d}{\mu} \rightarrow V = \frac{Re \cdot \mu}{\rho \cdot d} \tag{7}$$

Where: $V\ \left[\frac{\mathrm{m}}{\mathrm{s}}\right]$: magnitude of velocity, $\rho = 1.225\ \left[\frac{\mathrm{kg}}{\mathrm{m}^3}\right]$: density of air, $d = 0.01$ [m]: characteristic length, which is the cylinder diameter, $\mu = 1.7894 \cdot 10^{-5}\ \left[\frac{\mathrm{kg}}{\mathrm{m{\cdot}s}}\right]$: dynamic viscosity of air.

For both of the simulations the ‘Viscous Laminar’ model was applied. The air was assumed to be incompressible ideal gas. SIMPLE pressure-velocity coupling was used for the simulations, and second-order upwinding was set for the numerical schemes.

Both simulations were run in transient mode, thus, an appropriate time step value had to be determined for each of them. The time step values were determined based on the definition of the Courant number [11]:

$$\frac{V\Delta t}{\Delta x} \leq C_{max} \tag{8}$$

Where: $V\ \left[\frac{\mathrm{m}}{\mathrm{s}}\right]$: magnitude of velocity, Δt [s]: time step size, Δx [m]: smallest cell size in the domain in the direction of the flow.

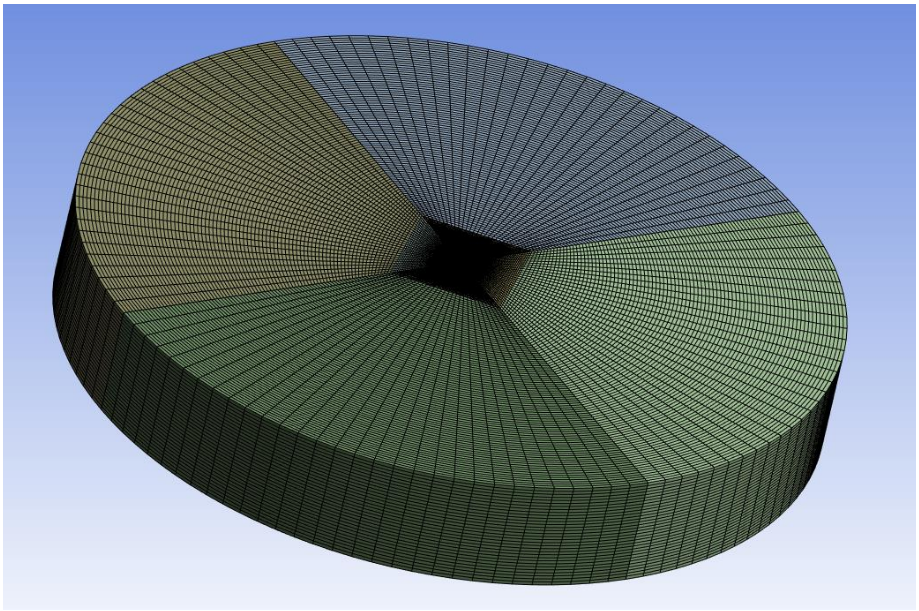

Fig. 3 The generated hexahedral mesh.

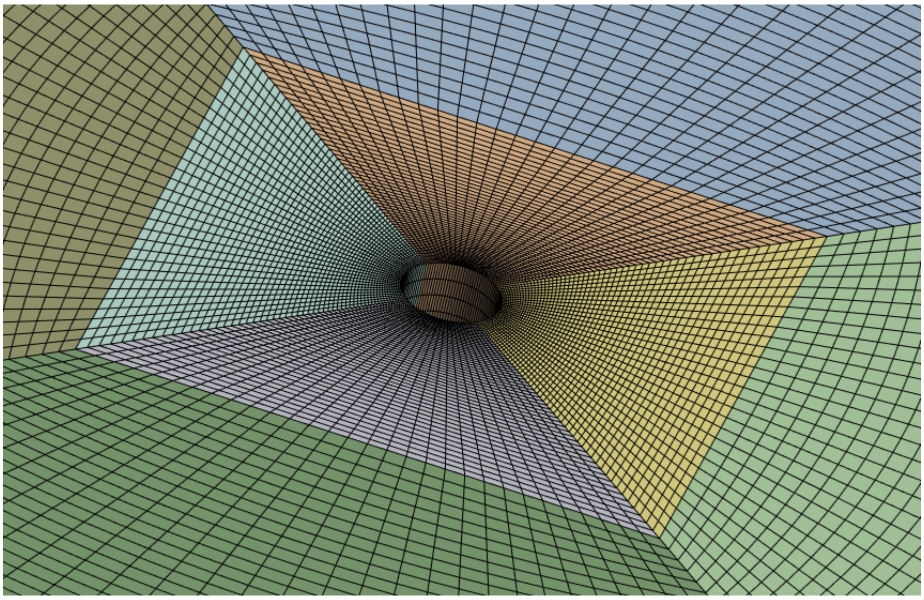

Fig. 4 The generated local mesh around the cylinder.

The simulation data for the two cases can be seen in Table 1. For the $Re = 100$ case (this was the first simulation) the maximum value of the Courant number was aimed to be around 1. However, from the simulation results ($C_{max} = 0.8$) it could be seen that the time step can be chosen to be higher than what is obtained with Eq. (8) for $Re = 60$, while still keeping the convergence of the simulation. For this simulation case the maximum value of the Courant number was: $C_{max} = 2.3$.

Table 1 Simulation data for the examined cases.

Reynolds numbers [-]	x-component of velocity [m/s]	y-component of velocity [m/s]	z-component of velocity [m/s]	Time step size [s]	Number of time steps [-]
60	0.0876	0	0	0.005	5500
100	0.1461	0	0	0.001	14000

It was necessary to prescribe the components of the inlet velocity because of the circular domain. This way the inlet velocity was purely x-directional.

The boundary conditions were set based on [10] and can be seen in Fig. 5. For the inlet and the outlet a velocity inlet, and a pressure outlet boundary condition were prescribed, respectively. For the upper and lower boundaries periodic boundary conditions were applied (in order to realize the infinitely long cylinder). The wall of the cylinder was specified as no-slip wall in order to bound fluid and solid regions.

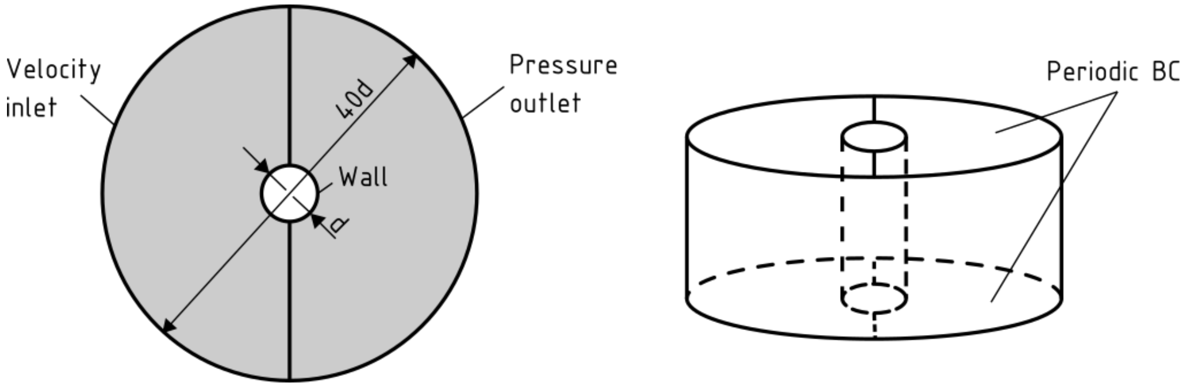

Fig. 5 The applied boundary conditions based on [10].

3.2 Results and discussion

The observed flow behaviors were in accordance with the expected results [12]. In the case of $Re = 60$ a laminar unstable wake could be observed. For a Reynolds number of 100 symmetric periodic vortex shedding occurred. In Fig. 6 and Fig. 7 the contour plots of the velocity magnitude can be seen in the x-y plane at $z = 0.03$ [m].

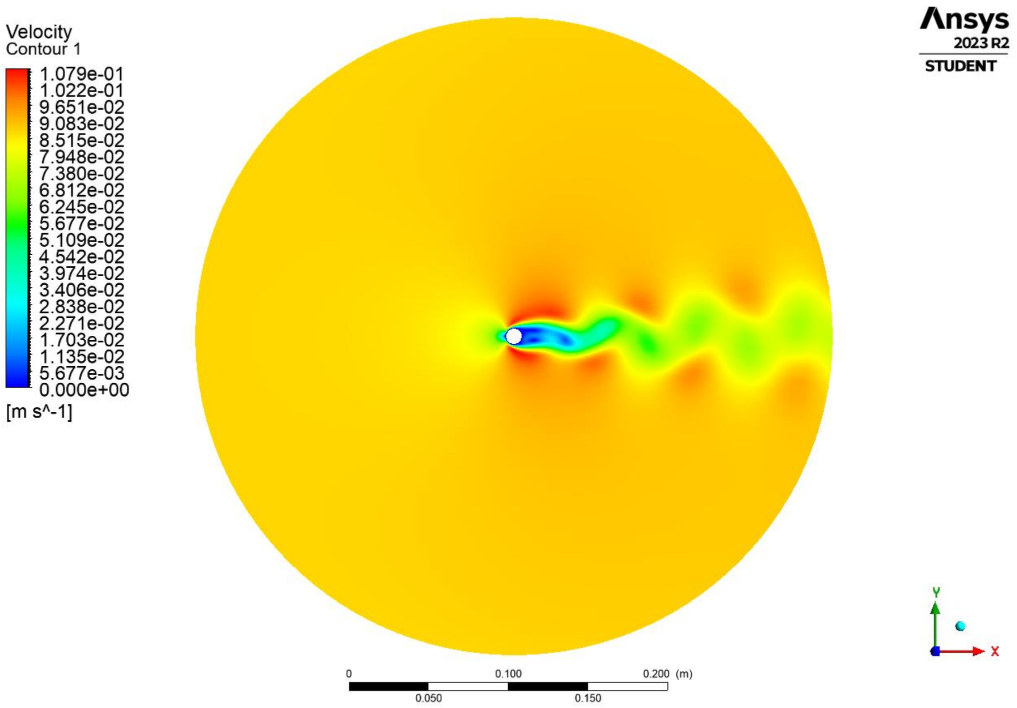

Fig. 6 Contour plot of the velocity magnitude at *Re* = 60.

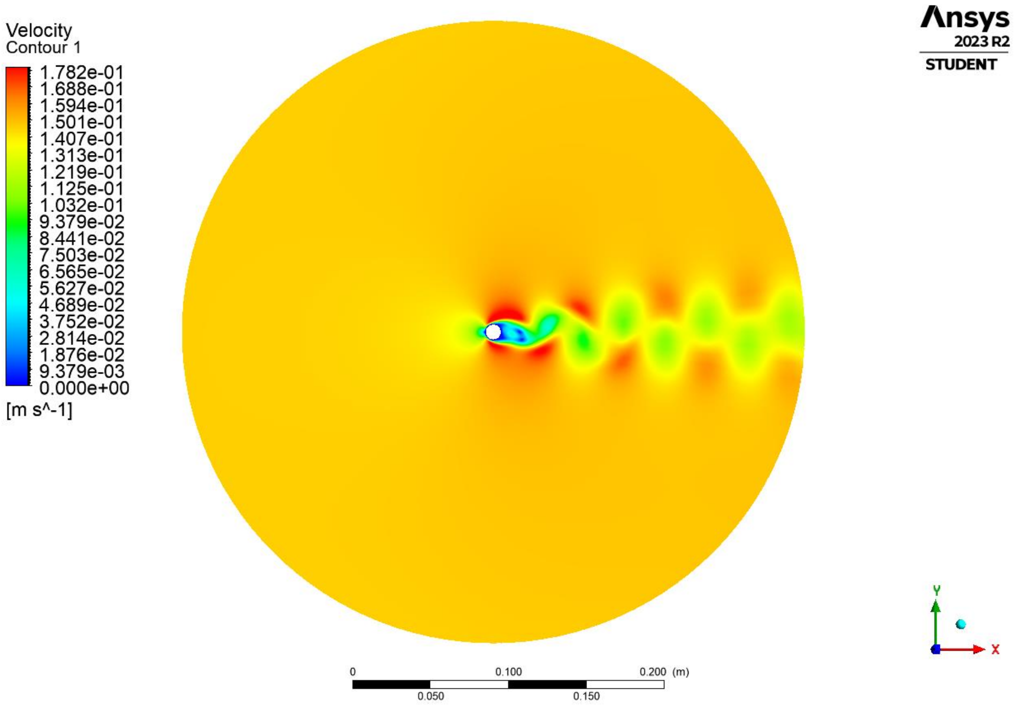

Fig. 7 Contour plot of the velocity magnitude at *Re* = 100.

For the validation of the simulation results different flow characteristics were examined. These were the following: RMS value of the lift coefficient $\left(c_{L,rms}\right)$, time-averaged value of the drag coefficient $(\bar{c}_D)$, and the Strouhal number (Sr).

The Strouhal number was calculated with the following formula [3]:

$$Sr = \frac{fd}{V} \tag{9}$$

Where: f [Hz]: vortex shedding frequency, which was obtained by the Fast-Fourier Transform (FFT) of the time signal of the lift coefficient, $d = 0.01$ [m]: characteristic length, which is the cylinder diameter, V $\left[\frac{\mathrm{m}}{\mathrm{s}}\right]$: magnitude of velocity.

The simulation results compared with the values taken from the literature [10] [13] (subscript ’lit’) can be seen in Table 2.

Table 2 Simulation results.

$\boldsymbol{Re}$ $[-]$	$\boldsymbol{c_{L,RMS}}$ $[-]$	$\boldsymbol{c_{L,RMS,lit}}$ $[-]$	$\boldsymbol{\bar{c}_D}$ $[-]$	$\boldsymbol{\bar{c}_{D,lit}}$ $[-]$	$\boldsymbol{Sr}$ $[-]$	$\boldsymbol{Sr_{lit}}$ $[-]$
60	0.09	0.09	1.42	1.38	0.14	0.14
100	0.24	0.18	1.35	1.33	0.17	0.16

It can be seen that the obtained simulation results are in great accordance with the literature data.

3.3 Vortex detection

3.3.1 Vortex detection at a Reynolds number of 100

As stated in the introduction, the main aim of the study with respect to the three-dimensional cylinder geometry is the detection of vortices, the parameter identification of the vortex detection parameters, and the comparison of the suggested parameter values with the results of the two-dimensional case [4].

Similarly to the two-dimensional study [4], the parameter identification at first was performed for the $Re = 100$ case, because for this Reynolds number the von Karman vortex street phenomenon holds. For a von Karman vortex there exists a theoretical value in the literature for the ratio of the coordinate differences of the neighboring vortex centers, this value is 0.281 [14]. Thus, by calculating these values for the different vortex pairs, the quality of the detection can be inspected.

One can see from Eq. (1) that it is required to set the temporal length of the integration. According to [4] the LAVD method requires at least two time steps to be able to perform the detection. However, it is not possible to increase the time steps unrestrictedly because after a while, fluid particles leave the domain, and the LAVD values can no longer be interpreted. In [4] it is stated that between the minimum and maximum integration time there is a time range within which the result is not significantly affected by the temporal length of the integration.

It is important to mention that every 10th time step from the CFD simulation was used for the vortex detection. The selected integration time, the number of time steps, and the number of files (this is different from the number of time steps, because as it was stated every 10th time step was used) used for the calculations can be seen in Table 3.

Table 3 Integration data for *Re* = 100.

Reynolds numbers [-]	**Temporal length of the integration [s]**	**Number of time steps [-]**	**Number of files [-]**
100	0.19	190	20

Since running the current code is a very time and memory consuming procedure, two vital considerations had to be made in order to be able to perform the vortex identification. At first, a much smaller domain had to be selected for the uniform grid than the original one in the simulation. The dimensionless coordinates bounding this region are the following (in the *z*-direction the whole domain bounded by the selected *x*- and *y*-coordinates was considered):

$$1.5\ [-] \le x/d \le 20\ [-] \tag{10}$$

$$-3\ [-] \le y/d \le 3\ [-] \tag{11}$$

This domain does not contain the cylinder and the region near the cylinder, because in this area the mesh is highly refined, thus, the interpolation would be significantly slower, and much more memory consuming if this region was considered also. The selected domain (denoted by a red rectangle) can be seen in Fig. 8.

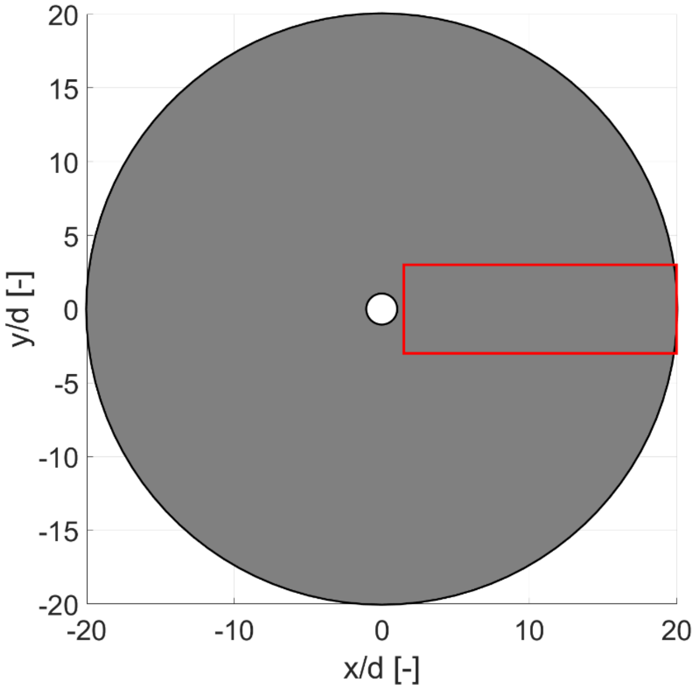

Fig. 8 The selected domain for the calculations.

In addition, the number of files had to be restricted at around 20 (as can be seen in Table 3), because otherwise the computer ran out of memory. As it was mentioned, between the minimum and maximum integration time there is a time range within which the result is not significantly affected by the temporal length of the integration. By choosing 20 files, the temporal length of the integration lies within said region. With this amount of files satisfactory results could be obtained. For this setup the running of the code took 906 seconds, so approximately 15 minutes, which is quite optimal from a practical point of view.

The parameter identification was performed for the same three vortex detection parameters as in [4]: *Nct*, *DeficiencyThresh* [%], *MinLength* [%]. *Nct* denotes the number of LAVD contour levels intended to extract. The *DeficiencyThresh* parameter is the maximum allowable convexity deficiency of the detectable vortices. The convexity deficiency of a closed curve in the plane is defined as the ratio of the area between the curve and its convex hull to the area enclosed by the curve [5]. The *MinLength* parameter is the minimum required perimeter of a vortex. If the perimeter of a given vortex falls below this threshold value, then it is going to be omitted. *MinLength* is expressed as a percentage of the cylinder diameter.

Firstly, the parameter identification was performed for the *Nct* parameter, while keeping the other two parameters at a constant value. Afterwards, with a suitable *Nct* value the parameter identification was performed for the other two vortex detection parameters also.

During the tuning of the parameters the same aspects were considered as in the two-dimensional case, namely: since the identification was based on the visual inspection of the detection results, a complete vortex row has to be detected, and the vortices should not be touching the surface of the cylinder. In addition, the realization of the 0.281 theoretical value was also inspected.

The suggested intervals for the parameters are the following: $Nct \in [100;200]$; $DeficiencyThresh \in [2;3]$ %; $MinLength \in [270;430]$ %. Within these intervals, the vortex detection results are similar to each other. The result of the vortex detection in the *x*-*y* plane at $z = 0.03$ [m] can be seen in Fig. 9. This figure is the contour plot of the LAVD values, where the red dots denote the centers, and the red, closed curves denote the boundaries of the vortices.

This result is similar to the two-dimensional one at *Re* = 120, presented in [4]. As it was stated beforehand, by checking the realization of the theoretical 0.281 value, the correctness of the vortex detection can be observed.

The ratios of the coordinate differences between the neighboring vortices are the following:

$$\frac{\Delta y_{12}}{\Delta x_{12}} = 0.4359\ [-], \qquad \frac{\Delta y_{23}}{\Delta x_{23}} = -0.3554\ [-] \tag{12}$$

$$\frac{\Delta y_{34}}{\Delta x_{34}} = 0.3192\ [-], \qquad \frac{\Delta y_{45}}{\Delta x_{45}} = -0.2306\ [-]$$

$$\frac{\Delta y_{56}}{\Delta x_{56}} = 0.2031\ [-], \qquad \frac{\Delta y_{67}}{\Delta x_{67}} = -0.2303\ [-]$$

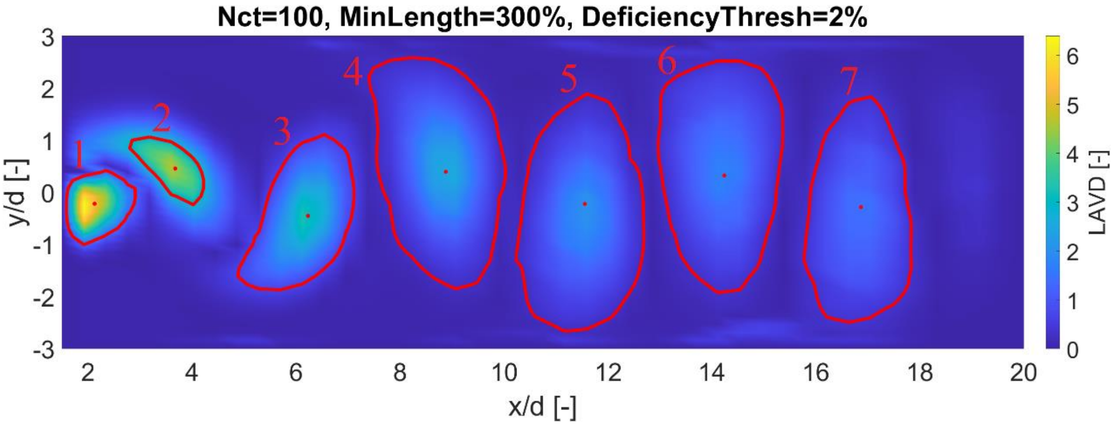

Fig. 9 Vortex detection with suggested parameters at *Re* = 100.

It can be seen that the calculated values slightly differ from the conceptual value. Nonetheless, the difference is not very significant, and it can also originate from the fact that the 0.281 value is a theoretical value with simplifications. It can be observed in Fig. 9 that a complete, symmetric vortex row has been detected.

Since the current example is a three-dimensional example, three-dimensional figures were also created with respect to the detected vortices. This can be seen in Fig. 10. This figure further reassures that a symmetric, coherent vortex row has been detected. It can also be seen that there is not any significant, observable variance along the *z*-axis.

As a next step, the current parameter tuning results were compared with the two-dimensional parameter identification results [4]. This can be seen in Table 4. One can see that the Reynolds numbers are not exactly the same for the two cases. The reason why $Re = 100$ was chosen for the three-dimensional simulation is because the flow structure is the same as for $Re = 120$, however, the author intended to compare the identification results for slightly different Reynolds numbers (while staying in the same flow regime). In order to compare a two-dimensional and a three-dimensional case for the same Reynolds numbers, in *Chapter 3.3.2* the Reynolds number will be 60 for both of the cases.

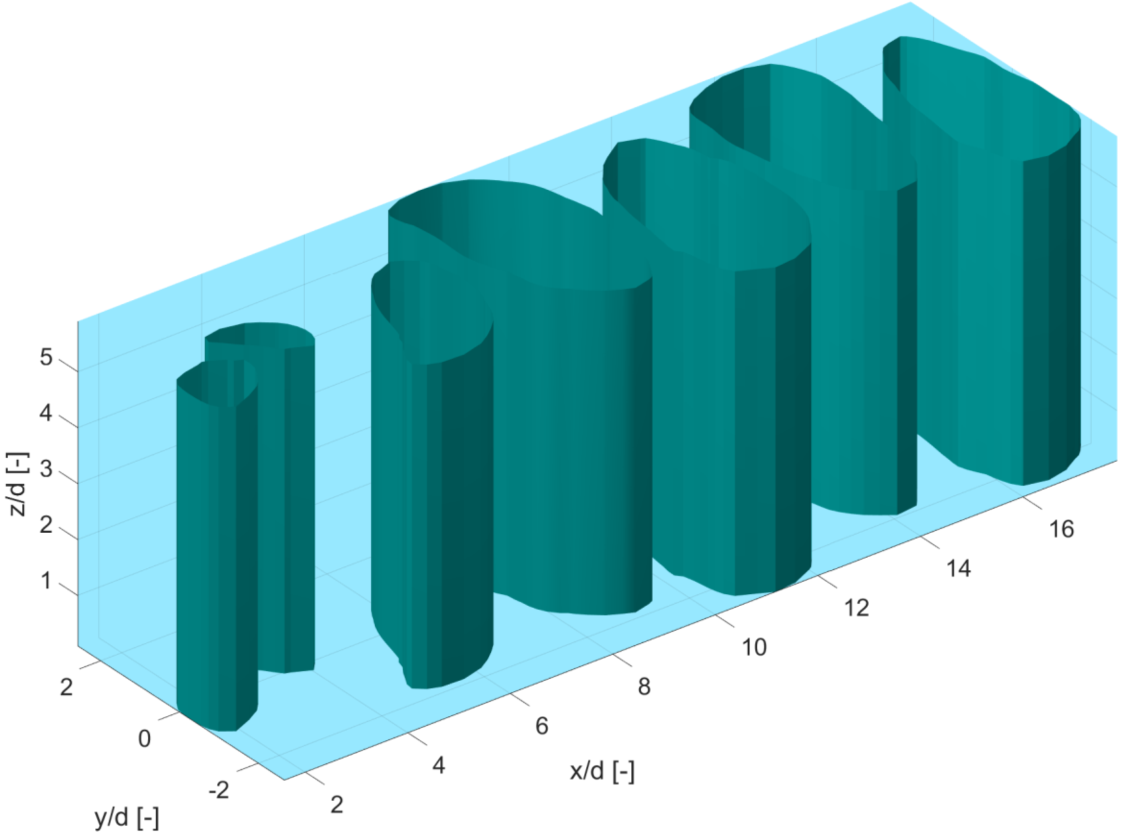

Fig. 10 Three-dimensional display of the vortex detection results.

Table 4 Comparison of the suggested intervals.

	***Re* = 100 (three-dimensional)**	***Re* = 120 (two-dimensional) [4]**	**∩**
***Nct* [-]**	[100;200]	[100;200]	[100;200]
***DeficiencyThresh* [%]**	[2;3]	[1;10]	[2;3]
***MinLength* [%]**	[270;430]	[75;180]	-

Based on the current results, and the results presented in [4], one can conclude that the [100;200] interval for the *Nct* parameter is indeed an optimal interval.

With respect to the *DeficiencyThresh* parameter a general suggestion cannot be formed because the suitable value for this parameter differs a little for every case. However, it can be advised based on the results to keep this value below 10%. Based on the visual inspection of the vortex detection results the further tuning of this parameter can be performed for the different cases more easily.

As for the *MinLength* parameter, its preferred value also varies for each case. On the other hand, it can be seen that its optimal value is not significantly higher or lower than the characteristic length of the body, this aspect is a good starting point when applying the current detection method for a given simulation and/or measurement data.

3.3.2 Vortex detection at a Reynolds number of 60

The parameter identification for this case is performed similarly to the previous one. The data with respect to the integration can be seen in Table 5.

Table 5 Integration data for *Re* = 60.

Reynolds numbers [-]	Temporal length of the integration [s]	Number of time steps [-]	Number of files [-]
60	0.95	190	20

The applied domain size is the same as before (in the *z*-direction also):

$$1.5\ [-] \leq x/d \leq 20\ [-] \tag{13}$$

$$-3\ [-] \leq y/d \leq 3\ [-] \tag{14}$$

The running of the code took 868 seconds which is approximately 14.5 minutes.

At first, the *Nct* parameter was examined, and afterwards the *DeficiencyThresh* and *MinLength* parameters were tuned. The suggested intervals for the different parameters, compared with the two-dimensional results [4] can be seen in Table 6.

Table 6 Comparison of the suggested intervals.

	***Re* = 60 (three-dimensional)**	***Re* = 60 (two-dimensional) [4]**	∩
***Nct* [-]**	[100;200]	[100;200]	[100;200]
***DeficiencyThresh* [%]**	[1;2]	[1;10]	[1;2]
***MinLength* [%]**	[190;480]	[60;495]	[190;480]

By comparing the current results with the results presented in [4], the preferred [100;200] interval for *Nct* is further reassured. As for the *DeficiencyThresh* parameter the same can be said as before, its suggested value differs a little for every case, however, by keeping it below 10%, and tuning it based on the visual inspection of the results, one can most certainly obtain the preferred vortex detection outcome. The *MinLength* parameter is in great accordance with the characteristic length. Therefore experimenting with values between e.g. 50% and 400% of the characteristic length can serve as a good starting point for obtaining satisfactory results.

The result of the vortex detection in the $z = 0.03\ [m]$ plane can be seen in Fig. 11. The three-dimensional visualization of the detected vortices has been performed for this case too, this can be seen in Fig. 12.

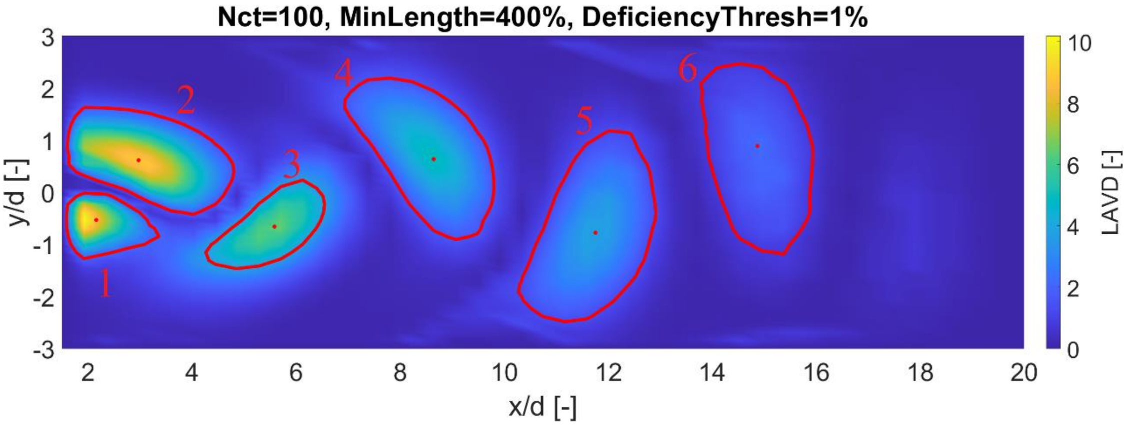

Fig. 11 Vortex detection with optimal parameters at *Re* = 60.

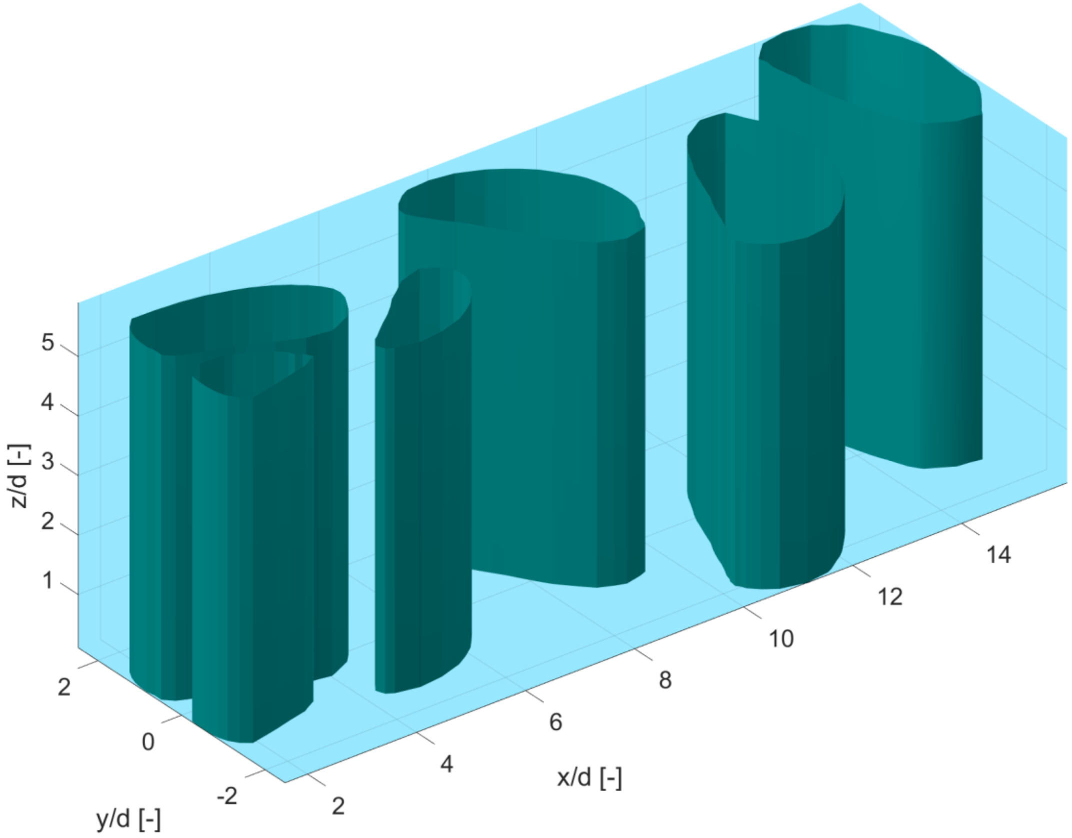

Fig. 12 Three-dimensional display of the vortex detection results.

The ratios of the coordinate differences between the neighboring vortices were determined for this case as well, these are the following:

$$\frac{\Delta y_{12}}{\Delta x_{12}} = 1.4121\,[-], \qquad \frac{\Delta y_{23}}{\Delta x_{23}} = -0.4878\,[-] \tag{15}$$

$$\frac{\Delta y_{34}}{\Delta x_{34}} = 0.4230\,[-], \qquad \frac{\Delta y_{45}}{\Delta x_{45}} = -0.4539\,[-]$$

$$\frac{\Delta y_{56}}{\Delta x_{56}} = 0.5344\,[-]$$

In [4] for a Reynolds number of 60, the whole vortex row exhibited complete symmetry (all of the absolute values were very close to each other). This is not entirely true for the current results. $\frac{\Delta y_{12}}{\Delta x_{12}}$ differs from the other ratios, nonetheless, this vortex pair is very close to the cylinder. It could be seen for $Re = 100$ also, that a little time is needed for the convergence of the ratios. Apart from $\frac{\Delta y_{12}}{\Delta x_{12}}$ the absolute values of the ratios are similar, and they become uniform faster than in the case of $Re = 100$ (the 0.281 theoretical value is not valid for this case since it only holds for a von Karman vortex street). It is worth mentioning, that in [4], the following ratios were obtained:

$$\frac{\Delta y_{12}}{\Delta x_{12}} = -0.4922\ [-], \qquad \frac{\Delta y_{23}}{\Delta x_{23}} = 0.4738\ [-] \tag{16}$$

$$\frac{\Delta y_{34}}{\Delta x_{34}} = -0.4938\ [-]$$

By excluding the $\frac{\Delta y_{12}}{\Delta x_{12}}$ ratio (from the current results, Eq. (15)), it can be seen from Eqs. (15)-(16) that the ratios are close to one another. Therefore, similarly to the 0.281 theoretical value, the said $\sim 0.4 - 0.5$ range seems to be characteristic of this particular vortex row structure.

4 Axial fan

4.1 Simulation setup

With respect to the axial fan geometry, three-dimensional steady RANS simulations using the frozen rotor model were carried out using ANSYS Fluent 22R2 software in [9] by Lendvai and Benedek. The applied turbulence model was Menter's k-ω SST turbulence model [9]. The air was assumed to be incompressible ideal gas [9]. Throughout the simulations, coupled pressure-velocity coupling was applied, and second-order upwinding was set for the numerical schemes [9]. The whole simulation domain can be seen in Fig. 13 a) and the enlarged inlet section can be seen in Fig. 13 b) [9].

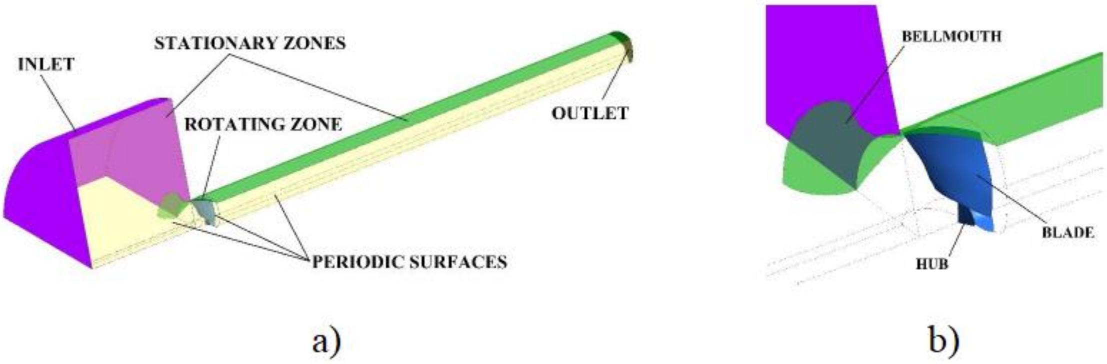

Fig. 13 The simulation domain used for the CFD simulations [9].

In order to reduce the computational cost, and the computational time, one blade was modeled with periodic boundary conditions [9]. The inlet included a bellmouth inlet acting as a baffle surface [9]. The outlet was positioned at the end of the long outlet duct $(20r_b)$, where: $r_b = 0.15$ [m] is the blade tip radius of the rotor. The rotating frame of reference was assigned to the blade passage domain, whereas the inlet and outlet domains remained steady [9]. In all simulations a constant total pressure was imposed on the inlet boundary, and the static pressure at the outlet was varied in accordance with measurements [9].

The surface mesh of the used numerical grid can be seen in Fig. 14 [9]. The free inlet and outlet duct sections featured structured H-grid meshes containing 913,000 and 770,000 elements, respectively [9]. The structured O-grid mesh for the rotating blade passage consisted of approximately 1.5 million hexahedral cells [9]. Above the hub, the blade passage was resolved with 110 elements in the axial and spanwise directions, and 122 elements in the pitch-wise direction [9]. The blade itself featured 80 and 90 cells in the spanwise and streamwise directions, respectively [9]. The blade tip gap was adequately resolved radially with 30 elements, and the blade thickness was modeled using 20 cells across [9].

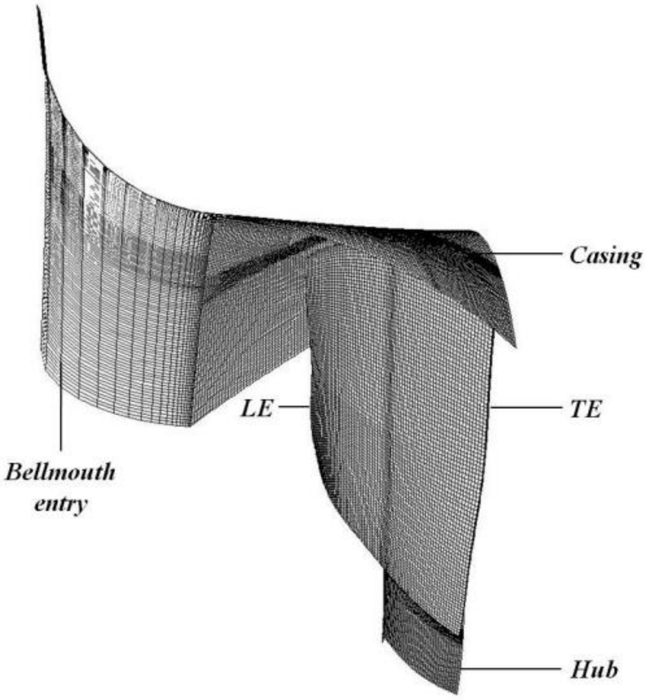

Fig. 14 The surface mesh of the used numerical grid [9].

In [9] apart from the CFD simulations, acoustic measurements were also carried out by Lendvai and Benedek. The CFD simulations were carried out at all operating points corresponding to the measurements [9]. These are seven operating conditions with flow rates between $\Phi = 0.34 - 0.26\ [-]$, which correspond to the pressure rise coefficients between $\Psi_s = 0.04 - 0.18\ [-]$ [9]. Where:

$$\Phi = \frac{Q_V}{u \cdot r_b^2 \cdot \pi} \tag{17}$$

$$\Psi_s = \frac{\Delta p_s}{\frac{\rho}{2} \cdot u^2} \tag{18}$$

Where: $\Phi\ [-]$ and $\Psi_s\ [-]$: global flow coefficient and global static pressure rise coefficient, $Q_V\ \left[\frac{\mathrm{m}^3}{\mathrm{s}}\right]$: volume flow rate, $u\ \left[\frac{\mathrm{m}}{\mathrm{s}}\right]$: blade tip peripheral velocity, r_b [m]: blade tip radius, Δp_s [Pa]: static pressure rise, $\rho\ \left[\frac{\mathrm{kg}}{\mathrm{m}^3}\right]$: density of air. The rotational speed was 1400 [rpm] for each case.

4.2 Results and discussion

Based on the results it was concluded that intensive tip leakage flow appears in all of the investigated cases [9]. By throttling the fan, the TLV origin moves upstream to the tip leading edge, and the exit angle of the TLV measured to the chord line increases [9]:

- $\Phi = 0.34$: the TLV develops near the mid-chord of the blade
- $\Phi = 0.31 - 0.28$: the TLV origin moves further upstream to the leading edge
- The TLV trajectory exit angle increase is observed for the $\Phi = 0.34 - 0.28$ region
- $\Phi = 0.28$: the exit angle increases to such an extent that the vortex core impinges on the consequent blade pressure surface, which leads to the so-called double leakage flow
- $\Phi = 0.26$: TLV trajectory is relatively independent of the operating conditions after impingement, but the throttling promotes the increase of strength and size of the TLV

4.3 Vortex detection

4.3.1 Banks' vorticity predictor-pressure corrector vortex core identification method

Simulation and vortex detection results with respect to one of the abovementioned simulations ($\Phi = 0.31$) were provided by Bálint Lendvai (PhD student at the Department of Fluid Mechanics, Faculty of Mechanical Engineering, Budapest University of Technology and Economics). The applied detection method was Banks' vorticity predictor-pressure corrector vortex core identification method [8].

This identification method uses predefined seed points to grow the vortex skeleton [8]. Starting from a seed point, the vortex detection algorithm in the first step predicts the vortex core direction based on the local vorticity vector [8]. However, the vorticity vector may not align with the vortex core [8]. Therefore, in the corrector step this prediction is corrected by searching for nearby pressure minimum in the plane perpendicular to the vorticity vector at the predicted point [8].

The described technique does not rely on numerical derivatives and the vortex skeleton is calculated based on local field variables only [8]. With the help of this vortex skeleton detection algorithm, the instantaneous vortex trajectories can be determined [8]. The detailed description, and other important aspects of the method can be found in [8].

The tip leakage vortex cores detected by Banks' vorticity predictor-pressure corrector method along with the fan geometry can be seen in Fig. 15.

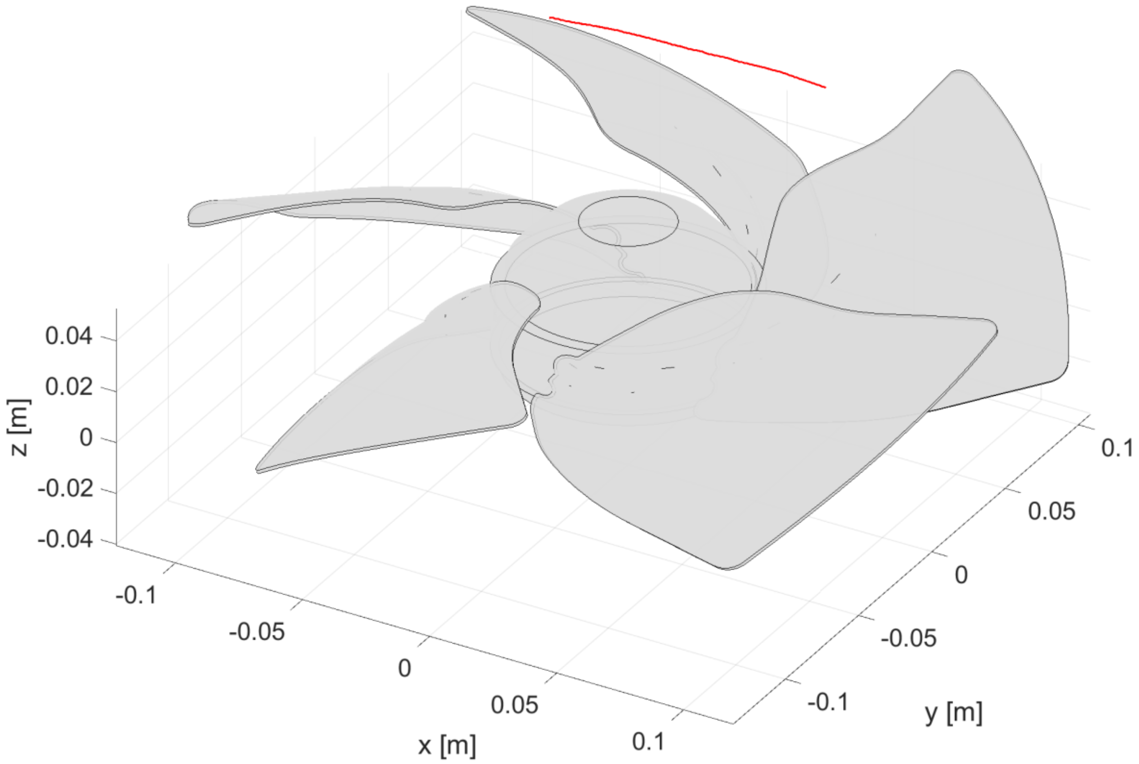

Fig. 15 Vortex centers detected with Banks' vorticity predictor-pressure corrector method.

4.3.2 LAVD vortex identification method

The advantage of the LAVD method compared to Banks' is that it uses only kinematic quantities, therefore it is applicable for compressible media, and it also offers information on the strength, and the size of the vortices besides the position of their cores.

Since the provided simulation results are in connection with a steady simulation, three time steps were utilized for the LAVD method, with an arbitrarily chosen 10^{-4} [s] time step value. Due to the size of the domain, and the number of nodes, the domain size had to be reduced significantly, due to the limited availability of computer memory. The numerical implementation of the method is in accordance with what is described in *Chapter 2.2*. The running of the code took 1549 seconds, which is approximately 26 minutes.

The main difference between the current and the circular cylinder case is the fact that for the axial fan, all of the vorticity components, meaning ω_x, ω_y and ω_z were considered. For the cylinder, only the dominant z-component of the vorticity was taken into account. By considering each component, it is not necessary to know the planes in which the vortices should be sought for. This makes the detection simpler and more general.

The vortex detection parameters were the following while determining the centers of the TLV along the z-axis: *Nct* = 100, *MinLength* = 12%, *DeficiencyThresh* = 6%. Where *MinLength* was non-dimensionalized by the chord length ($c = 0.124$ [m]). Comparing the parameter values to the previously detailed circular cylinder case, it can be seen that the *Nct* and *DeficiencyThresh* values are in great accordance with each other for the different geometries. The suggested value with respect to the *MinLength* parameter is smaller, than in the case of the cylinder. The tip leakage vortex cores detected by the LAVD method can be seen in Fig. 16.

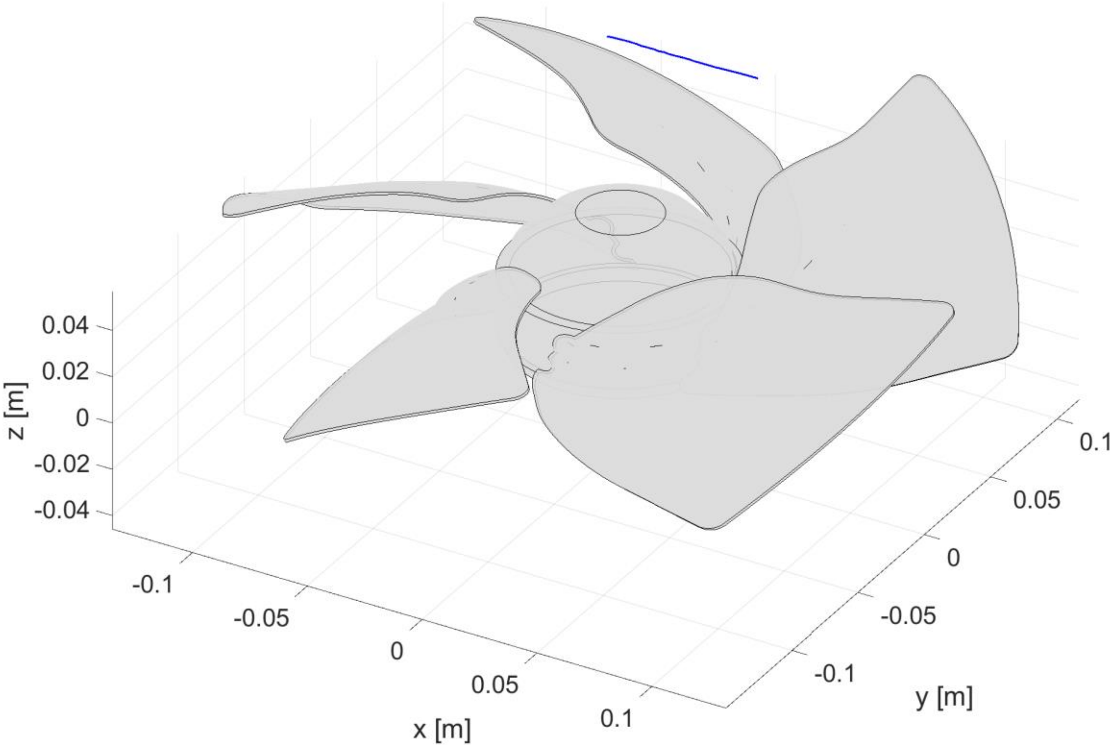

Fig. 16 Vortex centers detected with the LAVD method.

The comparison of the results can be seen in Fig. 17 and Fig. 18. It can be seen that the detection results are in great accordance with each other. In both cases, the TLV originates close downstream of the blade tip leading edge (LE) and then it propagates downstream in the blade passage.

It is important to mention that in the region close to the blades, due to the boundary layer, the vorticity has very high values (the LAVD values are also very high in this region), which can

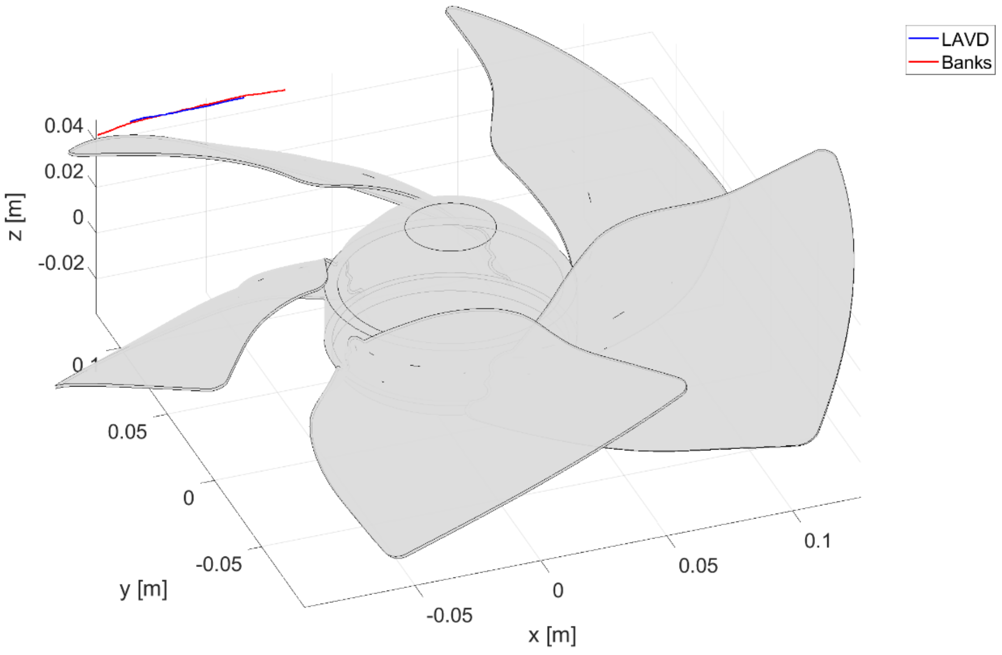

Fig. 17 Comparison of the TLV detection results.

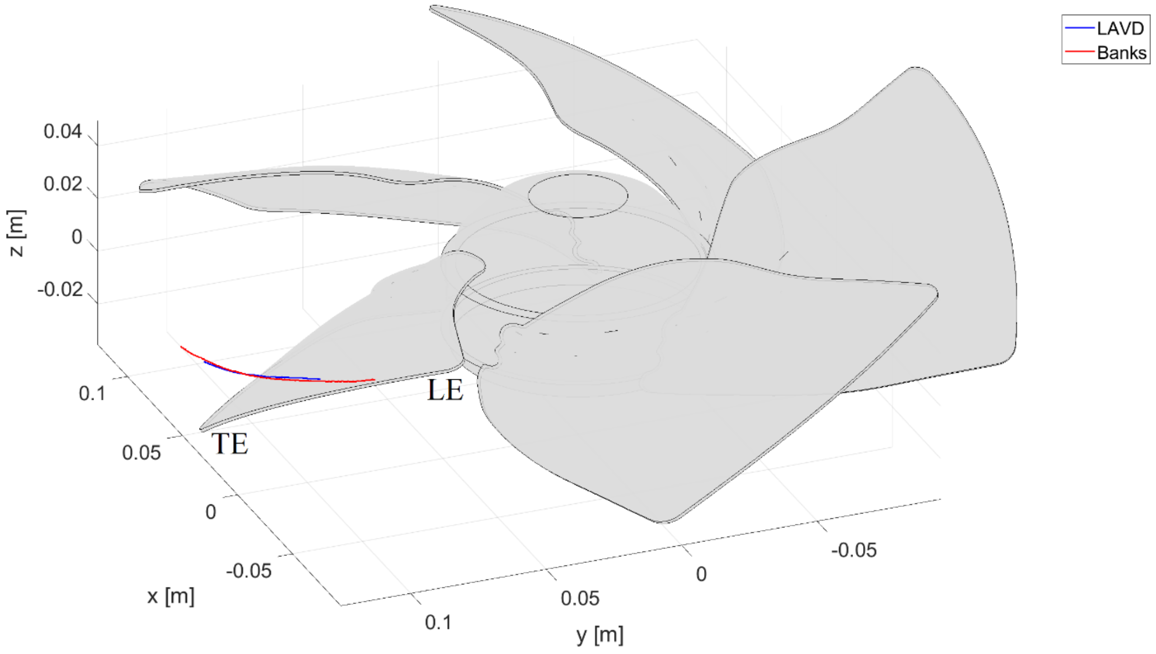

Fig. 18 Comparison of the TLV detection results from a different view.

cause problems in the detection of the TLV. As long as the TLV is substantially far from the vicinity of the blades, the vortices detected in the boundary layer can be eliminated by the proper adjustment of the vortex detection parameters.

However, when the TLV is close to the blades, the code can no longer distinguish these vortices, even is spite of the properly adjusted parameters. After this given point the TLV is detected together with the vortices in the boundary layer. Nonetheless, satisfactory results were obtained up until this critical point. In addition to the vortex centers the boundary of the TLV was also detected with the LAVD method in the different *x*-*y* planes along the *z*-axis. Some representative examples can be seen in Fig. 19-Fig. 23.

It can be seen from Fig. 19-Fig. 23 that the LAVD values are indeed higher in the region close to the blade. It can also be observed that the size of the TLV decreases as it gets closer to the blade. This is due to the fact that within a rotationally coherent Lagrangian vortex (as it was already mentioned) the LAVD values should decrease outwards, however, when the TLV gets closer to the blade the LAVD values start increasing quite close to the TLV, thus, explaining the smaller size of the vortex. One can also notice that the LAVD values remain approximately the same along the *z*-axis.

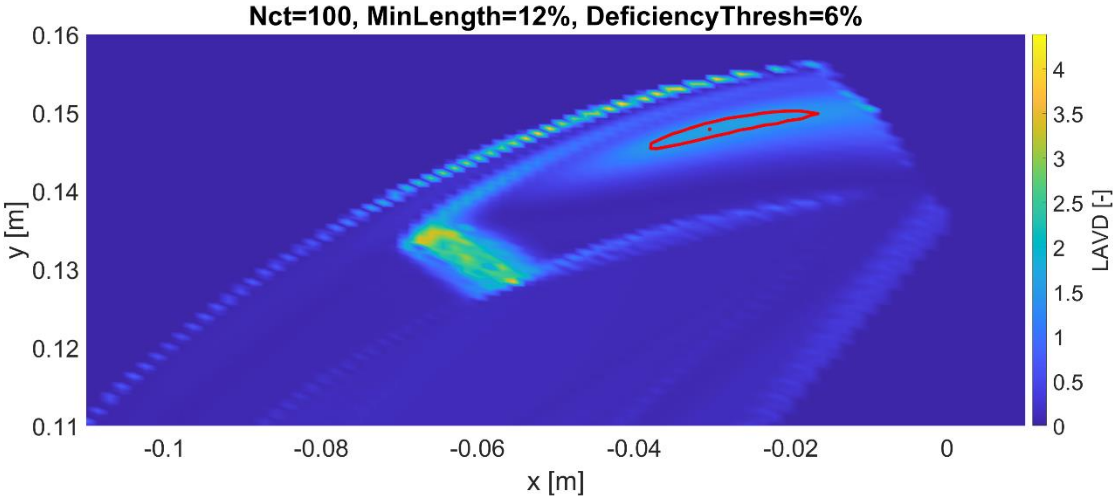

Fig. 19 TLV detected by the LAVD at *z* = 0.0316 [m].

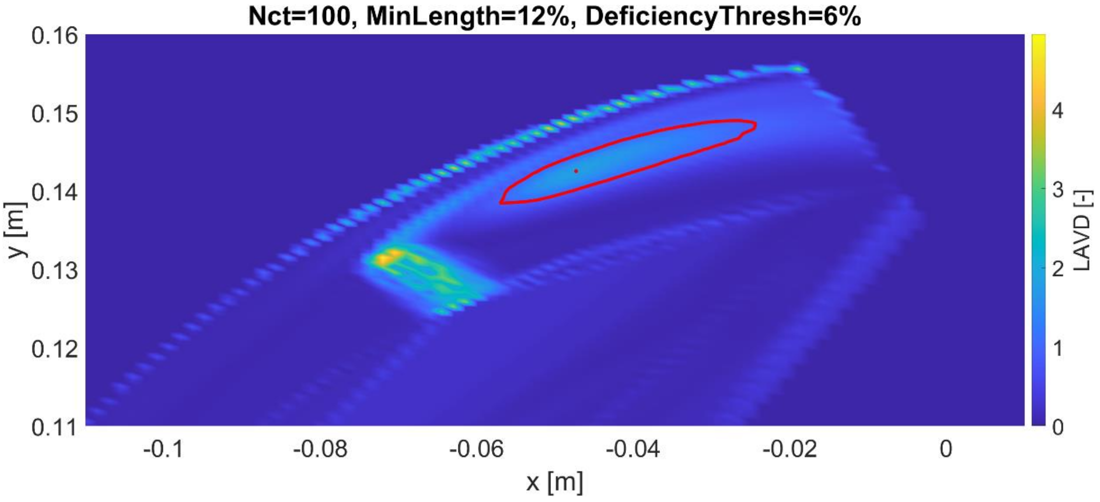

Fig. 20 TLV detected by the LAVD at *z* = 0.0347 [m].

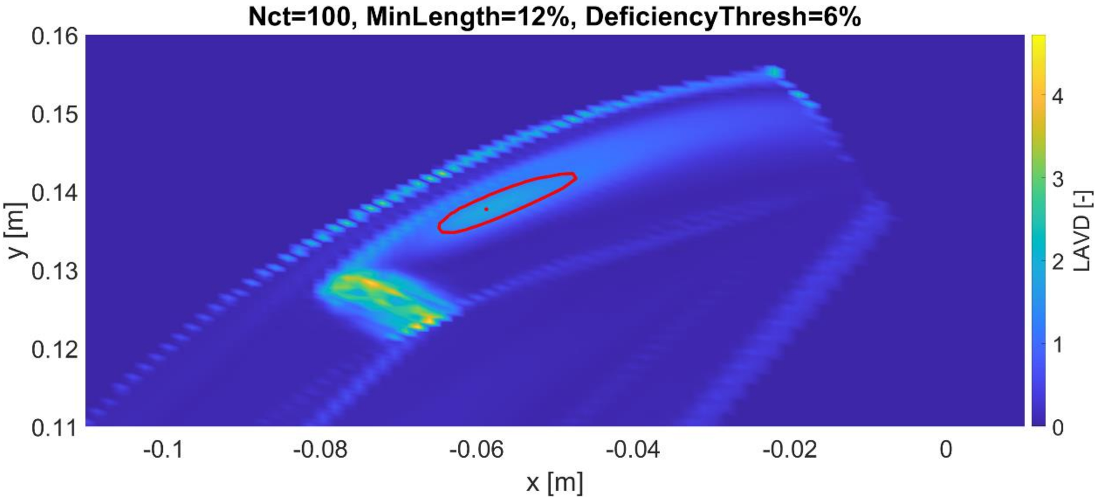

Fig. 21 TLV detected by the LAVD at *z* = 0.0378 [m].

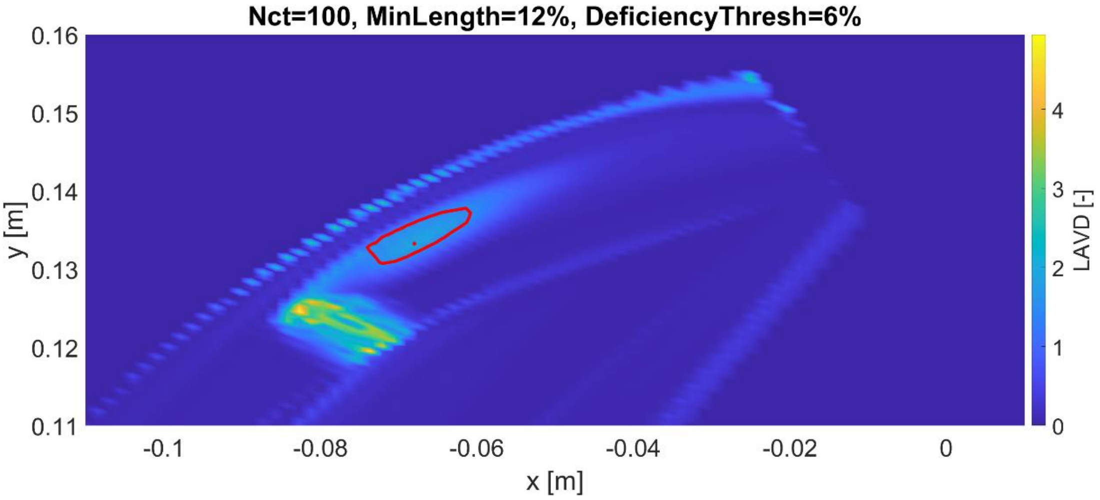

Fig. 22 TLV detected by the LAVD at *z* = 0.0408 [m].

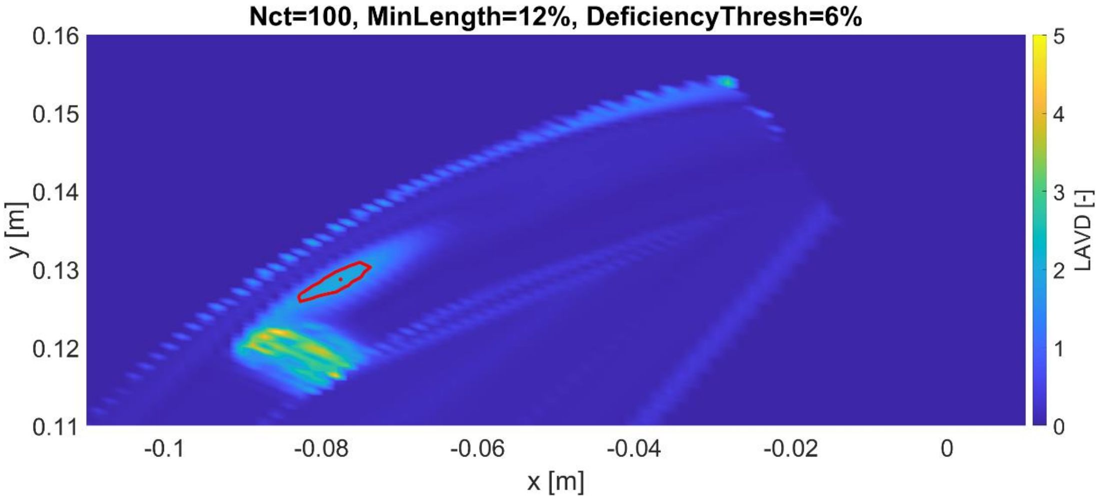

Fig. 23 TLV detected by the LAVD at *z* = 0.0439 [m].

The three-dimensional visualization of the TLV has also been performed by plotting the vortex boundaries in the *x-y* planes along the *z*-axis (only some of the detected boundaries were plotted for better observability), this can be seen in Fig. 24. The red curves denote the boundary, and the blue line denotes the center of the TLV.

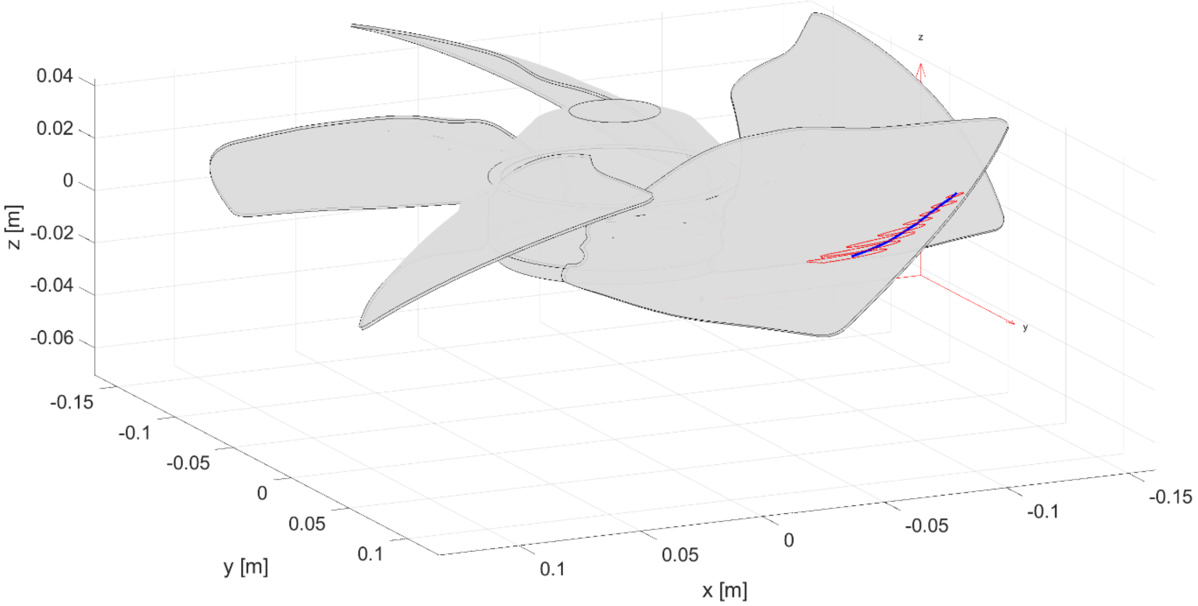

Fig. 24 Three-dimensional visualization of the TLV.

5 Summary of results

In the present work, vortex detection in three-dimensional flow around solid bodies with the LAVD vortex identification method was performed. The three-dimensional flows under investigation were the following: transient flow around a circular cylinder for two Reynolds numbers (60 and 100), and steady flow around an axial fan at $\Phi = 0.31$.

With respect to the circular cylinder the detection of the coherent vortex row, and the identification of the vortex detection parameters were successfully performed for both Reynolds numbers. In addition, the ratios of the coordinate differences between the neighboring vortices were also determined. For a Reynolds number of 100, the ratios were close to the conceptual 0.281 value. As for $Re = 60$, the ratios were similar to the previously determined values in the beforehand investigated two-dimensional case. These values were in the range of 0.4 to 0.5. This said interval can be representative of this particular vortex structure.

The determined suggested intervals were compared with the previously found results for the two-dimensional case. As a result of the comparison, it was suggested that the preferred value of the *Nct* parameter should be between 100 and 200, and the *DeficiencyThresh* parameter should be kept between 1% and 10%. As for the *MinLength* parameter, it is the hardest one to generalize, because its optimal value varies for every case. Nonetheless, by nondimensionalizing it with the characteristic value of the given geometry, and by the visual inspection of the results, preferred values can be determined, and with these values satisfactory detection results can be obtained. The three-dimensional visualization of the results was also provided for both cases.

With respect to the axial fan the aim was to detect the so-called tip leakage vortex, which is responsible for significant noise and loss generation both in household and industrial applications. The results were compared with detection results obtained by Banks' vorticity predictor-pressure corrector vortex core identification method, provided by Bálint Lendvai. The advantage of the LAVD method compared to Banks' is that it uses only kinematic quantities (thus, it is applicable for compressible media), it also offers information on the strength, and on the size of the vortices besides the position of their centers. The obtained vortex core results were in great accordance with each other. The results showed that the TLV originates close downstream of the blade tip leading edge and then it propagates downstream in the blade passage. The three-dimensional visualization of the TLV was also provided in the paper.

Acknowledgement

I would like to thank my advisor Dr. Balla Esztella, without whom the current research would not have been possible. I would also like to thank Bálint Lendvai for his constant help and support, and for providing the axial fan simulation data, and the vortex detection results obtained with Banks' method.

Project no. 143204 has been implemented with the support provided by the Ministry of Innovation and Technology of Hungary from the National Research, Development and Innovation Fund, financed under the OTKA K 22 funding scheme.

Supported by the ÚNKP-23-2-I-BME-59 New National Excellence Program of the Ministry of Culture and Innovation from the source of the National Research, Development, and Innovation Fund. Project no. TKP-6-6/PALY-2021 has been implemented with the support provided by the Ministry of Culture and Innovation of Hungary from the National Research, Development and Innovation Fund, financed under the TKP2021-NVA funding scheme.

References

[1] Nguyen, C. H., Nguyen, D. T., Owen, J. S., Hargreaves, D. M. "Wind tunnel measurements of the aerodynamic characteristics of a 3:2 rectangular cylinder including non-Gaussian and non-stationary features", Journal of Wind Engineering and Industrial Aerodynamics, Volume 220, 2022. https://doi.org/10.1016/j.jweia.2021.104826

[2] Arunachalam, S., Lakshmanan, N. "Across-wind response of tall circular chimneys to vortex shedding", Journal of Wind Engineering and Industrial Aerodynamics, Volume 145, pp. 187-195, 2015. https://doi.org/10.1016/j.jweia.2015.06.005

[3] Lajos Tamás. "Az áramlástan alapjai", Műegyetemi Kiadó, Budapest, 2019.

[4] Kovács, K. A., Balla, E. "Parameter identification of the Lagrangian-averaged Vorticity Deviation Vortex Detection Method Through the Investigation of Fluid Flow Around Solid Bodies", Periodica Polytechnica Mechanical Engineering, 2023. https://doi.org/10.3311/PPme.22874

[5] Haller, G., Hadjighasem, A., Farazmand, M., Huhn, F. "Defining coherent vortices objectively from the vorticity", Journal of Fluid Mechanics, Volume 795, pp. 136-173, 2016. https://doi.org/10.1017/jfm.2016.151

[6] Ansys "Ansys Workbench, (23.2)", [computer program] Available at: https://ww.ansys.com/academic/students/ansys-student [Accessed: 5 August 2023]

[7] The MathWorks "MATLAB, (9.14)", [computer program] Available at: https://www.mathworks.com/products/new_products/release2023a.html [Accessed: 14 September 2023]

[8] Lendvai, B. Benedek, T. "Application of a vortex identification method for quantifying the tip leakage vortex wandering in a low-speed axial fan case study", 15th European Conference on Turbomachinery Fluid Dynamics and Thermodynamics, 2023.

[9] Lendvai, B. Benedek, T. "Experimental and numerical investigation of the blade tip-related aeroacoustic sound source mechanisms of a ducted low-speed axial flow fan", Applied Acoustics, accepted, in press, 2023.

[10] Rajani, B.N. Kandasamy, A. Majumdar, S. "Numerical simulation of laminar flow past a circular cylinder", Applied Mathematical Modelling, Volume 33, pp. 1228-1247, 2008. https://doi.org/10.1016/j.apm.2008.01.017

[11] Dr. Kristóf Gergely. "Áramlások numerikus modellezése", Akadémiai Kiadó, Budapest, 2019. https://mersz.hu/kristof-aramlasok-numerikus-modellezese//

[12] Schlichting, H., Gersten, K. "Boundary-Layer Theory", Springer, Heidelberg, 2016. https://doi.org/10.1007/978-3-662-52919-5

[13] Qu, L., Norberg, C., Davidson, L., Peng, S.H., Wang, F. "Quantitative numerical analysis of flow past a circular cylinder at Reynolds number between 50 and 200", Journal of Fluids and Structures, Volume 39, pp. 347-370, 2013. https://doi.org/10.1016/j.jfluidstructs.2013.02.007

[14] Glauert, H. "The Elements of Aerofoil and Airscrew Theory", Cambridge University Press, Cambridge, 1947. https://doi.org/10.1017/CBO9780511574481